

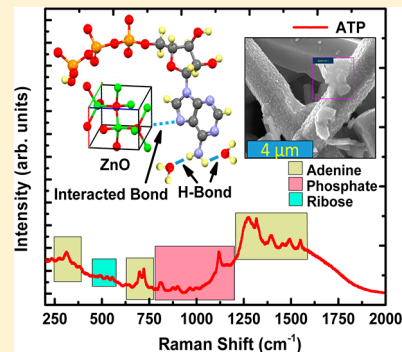
Probing the Interaction at the Nano–Bio Interface Using Raman Spectroscopy: ZnO Nanoparticles and Adenosine Triphosphate Biomolecules

A. Bhaumik,[†] A. M. Shearin,[†] R. Delong,[‡] A. Wanekaya,[§] and K. Ghosh^{*,†}

[†]Department of Physics, Astronomy and Materials Science, [‡]Department of Biomedical Science, and [§]Department of Chemistry, Missouri State University, Springfield, Missouri 65897, United States

Supporting Information

ABSTRACT: With the advent of nanobiotechnology, there will be an increase in the interaction between engineered nanomaterials and biomolecules. Nanoconjugates with cells, organelles, and intracellular structures containing DNA, RNA, and proteins establish sequences of nano–bio boundaries that depend on several intricate complex biophysicochemical reactions. Given the complexity of these interactions, and their import in governing life at the molecular level, it is extremely important to begin to understand such nanoparticle–biomaterial association. Here we report a unique method of probing the kinematics between an energy biomolecule, adenosine triphosphate (ATP), and hydrothermally synthesized ZnO nanostructures using micro Raman spectroscopy, X-ray diffraction, and electron microscopy experiments. For the first time we have shown by Raman spectroscopy analysis that the ZnO nanostructures interact strongly with the nitrogen (N_7) atom in the adenine ring of the ATP biomolecule. Raman spectroscopy also confirms the importance of nucleotide base NH_2 group hydrogen bonding with water molecules and phosphate group ionization and their pH dependence. Calculation of molecular bond force constants from Raman spectroscopy reinforces our experimental data. These data present convincing evidence of pH-dependent interactions between ATP and zinc oxide nanomaterials. Significantly, Raman spectroscopy is able to probe such difficult to study and subtle nano–bio interactions and may be applied to elegantly elucidate the nano–bio interface more generally.



INTRODUCTION

The interface between nanomaterials and biomolecules initiates comprehension of a new science concerned with the innocuous use of nanotechnology and nanomaterials for “nano–bio” applications. The interface encompasses vibrant physicochemical interactions, kinetics, and thermodynamic exchanges.^{1–3} The dynamic forces and molecular components modeling these interactions must be understood for better study of these intricate interfaces. Extensive applications have made the research of the interaction between nanomaterials and biomolecules of significant interest in the past couple of years.^{4–6} The ability of nanomaterials to interact with biomolecules depends on various factors. The interaction kinematics may be determined by the nanoparticle’s characteristics, including the chemical composition, porosity, and surface crystallinity.^{1,7–9} Three different dynamic surfaces important for the nano–bio interface are the nanoparticle’s surface, the solid–liquid interface, and the contact zone with an organic molecule.⁸

ZnO nanoparticles are nontoxic, biosafe, and biocompatible,¹⁰ thereby rendering them useful in applications concerning drug carriers, cosmetics, and medicinal materials.^{11–13} A recent study showed that low concentrations of ZnO nanoparticles did not cause cellular damage and poly(vinyl alcohol) (PVA)-coated ZnO nanoparticles had the ability to be internalized by bacterial cells, affirming the belief of ZnO as a drug delivery option.¹⁴ Finally, ZnO is strongly Raman active, thereby rendering

it a good candidate for studying binding capabilities with biomolecules.^{15,16} Rumyantseva et al. confirm the use of ZnO nanocrystals for ultrasensitive detection of biomolecules by micro Raman scattering experiments.¹⁶ Hydrothermally synthesized ZnO nanostructures with varied morphology and surface properties^{17,18} provide an idealistic model to determine the interaction kinetics with biomolecules. Adenosine triphosphate (ATP) plays an essential role in biological energy transfer reactions.¹⁹ Previous studies have shown that iron(III) has the ability to bind to ATP and adenosine monophosphate (AMP) by studying Raman spectral lines.²⁰ Lanir et al. has further explored the interaction between ATP and divalent metal ions under different pH conditions.²¹ Rimai et al. has done extensive work on ATP’s Raman spectra and has explored its dependence on pH.²²

Vibrational spectra can give comprehensive information concerning the molecular conformation and can be obtained by either direct absorption or micro Raman spectroscopy. Strong limitations are placed on the use of direct absorption by the properties of water in infrared spectroscopy. Raman spectroscopy has become much more precise in recent years and is being widely used for studying diverse biomolecules.^{23–25} Previous interaction studies have concentrated on

Received: June 22, 2014

Revised: July 17, 2014

Published: July 29, 2014

the phosphate moiety, which is known to interact strongly with all metal cations.^{19–21} This study attempts to revisit the reactions at the interface between ZnO nanoparticles and ATP biomolecules at all the possible moieties in ATP by employing micro Raman spectroscopy. The findings of this research may have important applications in the study of ATP reactions with nanoparticles.

■ EXPERIMENTAL PROCEDURES

All the chemicals used in this research were analytic grade reagents. The experimental details are as follows: A 0.15 M concentration of $\text{Zn}(\text{NO}_3)_2 \cdot 6\text{H}_2\text{O}$ (GFS Chemicals, assay 98.0–102.0%) was dissolved in 20 mL of deionized HPLC water (GFS Chemicals, resistivity at 25 °C of 18.0 M Ω cm) under stirring. NH_4OH (GFS Chemicals, concentration 10.0 ± 0.5% (v/v)) was added to the resulting aqueous solution until the pH of the solution was 9. The solution was then transferred into Teflon-lined stainless steel autoclaves, sealed, and maintained at a reaction temperature of 200 °C for 15 h. Addition of (10 mL) ethylene glycol (EG) (GFS Chemicals, 99% pure) to the aqueous solution was done before hydrothermal treatment was carried out. After the completion of the hydrothermal process, the solid products were centrifuged (LW Scientific centrifuge, model E8) at a rotation speed of 30 revolutions s⁻¹ for 30 min. The solution was washed three times with distilled water and ethyl alcohol (Fisher Scientific, anhydrous and denatured) to remove the ions remaining in the final product and finally dried at 100 °C in air. Thus, the ZnO nanostructures were synthesized by an energy effective hydrothermal technique. The interaction studies of ATP with ZnO nanorods were carried out using the following process: A 40 mg mass of as-synthesized ZnO nanorods were mixed into 600 μL of deionized HPLC water and 6 mg of ATP (Sigma-Aldrich, anhydrous basis, assay >99%) was mixed into 150 μL of deionized (DI) water to form their respective solutions. The solutions were sonicated for 5 min to uniformly distribute the constituents in solution. The ATP mixture was separated into three 50 μL portions. The ZnO mixture was separated into four 150 μL portions. Four mixture samples were prepared and are referred to as samples A, B, C, and D in this paper. Sample A contains only 150 μL of ZnO, whereas the rest of the samples contain 200 μL of the ZnO and ATP mixture. A 10 μL volume and a 15 μL volume of 1 N HCl (GFS Chemicals, concentration 1 ± 0.001 N) were added to samples C and D, respectively. The samples were stored at room temperature for 1 day in a desiccator. The samples were sonicated for 10 min in deionized HPLC water to remove the loosely interacting constituents. The ATP biomolecules loosely bound to the ZnO nanoparticles tended to detach themselves during the sonication process. We were particularly interested to study the Raman spectroscopy of the ATP biomolecules attached onto the surface of the ZnO nanostructures. The solid products were precipitated out and dried in air for further ZnO–ATP interaction studies.

The powder X-ray diffraction patterns of the obtained samples were characterized by employing X-ray diffraction (XRD; Bruker, D8 Discover; θ –2 θ scan with $\text{Cu K}\alpha$ ($\lambda = 1.5405 \text{ \AA}$)). Rietveld refinements were carried out using Diffrac^{plus} Topas software. The vibrational phonon modes were investigated by micro Raman spectroscopy using a 785 nm laser (Horiba Labram Raman-PL). The Raman spectra were analyzed using Gaussian and Lorentzian peak fittings with NSG Lab spec software. The morphology and elemental analysis of the as-prepared samples

were determined by scanning electron microscopy (FEI Quanta 200S).

■ RESULTS AND DISCUSSION

XRD Analysis of ZnO Nanostructures. The XRD patterns of hydrothermally synthesized ZnO nanostructures were characterized using X-ray powder diffraction (Bruker, D8 Discover; θ –2 θ scan with $\text{Cu K}\alpha$ ($\lambda = 1.5405 \text{ \AA}$)). Rietveld refinements were carried out by employing Diffrac^{plus} Topas software. Extreme care was taken for precise collection of XRD data by minimizing background influence, asserting the correct peak-shape profile function, refinement of the peak profile limits as well as the structural limitations, and good interpretation of the agreement indices (*R* values) during the refinement procedures. The powdered sample was placed according to the Bragg–Brentano reflection geometry during XRD experiments. Prior to the collection of XRD data, certain critical conditions were considered, namely, the geometry of the XRD instrument, all axis alignment of the samples, correct calibrations of the XRD instrument, the sample thickness, the primary and secondary slit sizes, and a suitable data acquisition time. The condition that is a prerequisite for a satisfactory Bragg–Brentano geometry is that the incident X-ray beam must fall on the powdered sample at all possible angles to guarantee a constant-volume condition. Commonly wide divergence slits are used, and thereby, the X-ray beam strikes the sample holder at low angles, therefore reducing the intensities of the diffracted beam.²⁶ Keeping in mind the above-mentioned problem, we have employed 0.6 mm wide primary and secondary divergence slits. Ensuring good counting statistics during the collection of XRD data at high diffraction angles, we have used a 6 s counting time. The Bragg–Brentano reflection geometry assumes the sample to be infinitely thick, so we have spent a considerable time making thicker powder samples for XRD. The calculated goodness of fit (GOF) from the Rietveld refinement appreciably approached 1 after proper corrections employing spherical harmonics. Smoothing the XRD plot was particularly restricted before refinement procedures to prevent point-to-point correlations which result in a considerable error during the refinement process. To be quite precise with the refinement parameters, the emission profile was measured for all possible $\text{Cu K}\alpha$ radiations. An order of 5 was employed in Chebychev background correction. The goniometer radius was carefully incorporated in the program considering the primary and secondary soller slits used. For better refinement results zero error and absorption correction factors were also considered. The Lorentz polarization factor was not refined during the refinement process. The peak profile function employed for refinement was the fundamental parameter (FP). FPs have a high degree of accuracy as they comprise a mixture of Lorentzian and Gaussian functions convoluted with straight line segments. The parameters used in the FPA model are physically based on the geometry of the diffractometer, thereby rendering better refinement values. This enables improved understanding of the line profile model fit.²⁷ Refinements of space coordinates and Debye–Waller temperature factors were restricted during Rietveld analysis. The number of variable parameters was carefully chosen to avoid anomalous refinement results. First, Pawley fitting (unrestrained fitting of parameters) was used to determine the lattice parameters, which were not refined in subsequent Rietveld refinements.

Powder XRD was carried out on all four samples (A, B, C, and D). Rietveld analysis of the XRD data was done to analyze

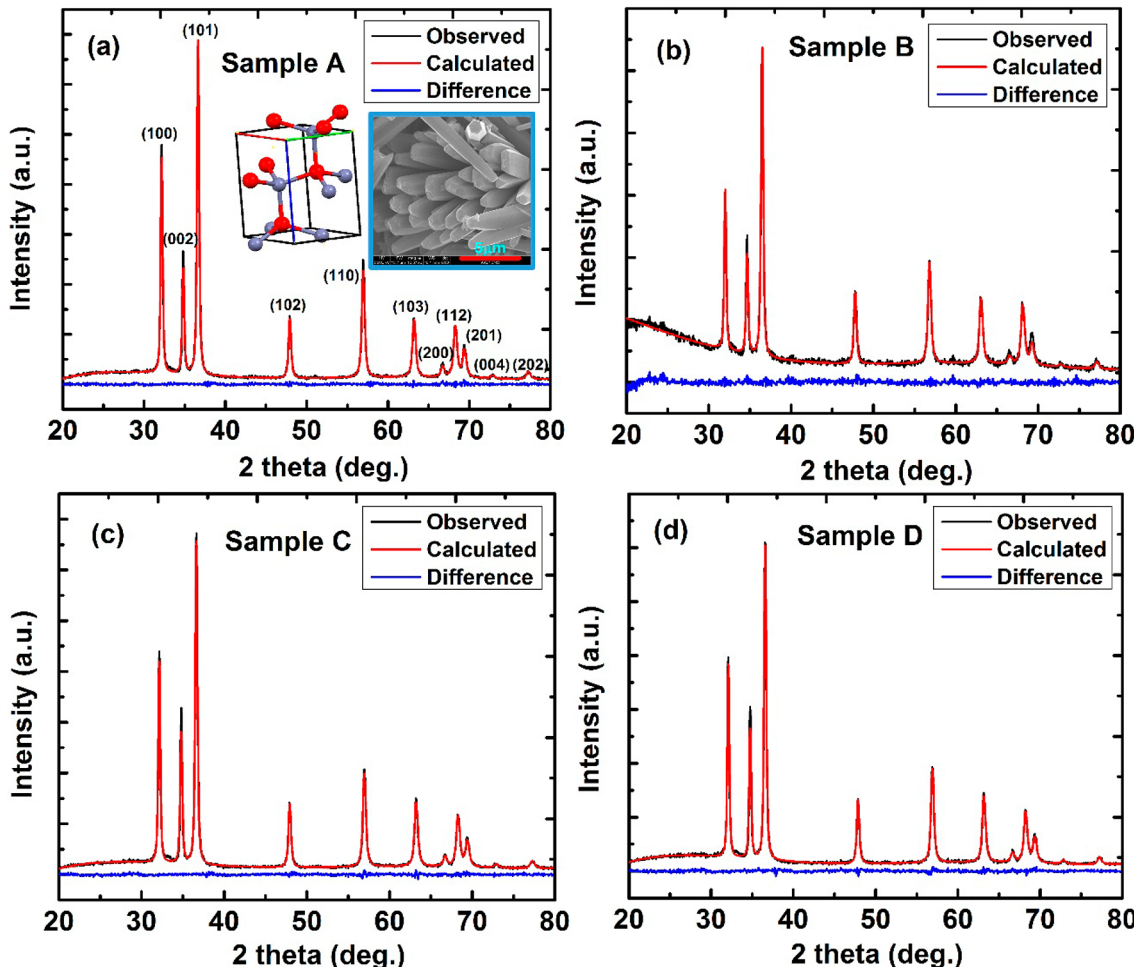


Figure 1. Rietveld-analyzed X-ray diffraction patterns of (a) sample A (ZnO + HPLC water), (b) sample B (ZnO + HPLC water + ATP), (c) sample C (ZnO + HPLC water + ATP + 10 μ L of 1 N HCl), and (d) sample D (ZnO + HPLC water + ATP + 15 μ L of 1 N HCl).

the XRD peaks. The observed, calculated (by Rietveld refinement), and difference XRD patterns are represented in Figure 1 by black, red, and blue colors, respectively. The XRD plot is indicative of the crystallographic structure of ZnO. It clearly shows that ZnO crystallizes as *P6₃mc* (hexagonal close-packed crystal structure). The calculated *c/a* ratio indicates negligible crystal strain in the interacting samples of ZnO. Absence of impurity peaks in the XRD plot rules out the presence of any secondary phases after interaction.

Raman Spectroscopy of ATP. The Raman spectra of pure ATP consist of two distinct sets of peaks: one characteristic of adenine ring vibrations and the other characteristic of the triphosphate modes. Raman scattering from the ribose moiety is generally very weak.²² Figure 2a represents the Raman spectra of pure ATP along with the shaded regions representative of the moieties present in the energy biomolecule. Thus, specific interactions of triphosphate and adenine moieties can be monitored simultaneously. The first Raman studies of the binding of divalent metal entities with the triphosphate moiety of ATP were reported by Rimai et al.^{28–30} In this study we focus our attention on the interaction of ZnO nanostructures with the different moieties of ATP at neutral and acidic levels of solutions. Raman microscattering techniques do not suffer any restriction and are capable of revealing different modes of binding between metal oxides and the adenine moiety such as direct coordination (e.g., at N₁, N₇,

or –NH₂) or charge transfer complex formation.³¹ The five probable nitrogen binding sites in the adenine entity are the pyrimidine N₁ and N₃ and imidazole N₇ and N₉ ring nitrogens and exocyclic –NH₂. The C=C bond can play an active role in binding too.³² Reviewing the interaction of the adenine entity with divalent metal ions may illustrate a better understanding of the N donors in binding.

Hydrolysis of ATP. Figure 2b represents the Raman spectra of hydrolyzed ATP. Dissolution of ATP involves formation of hydrogen bonds with water molecules, and a significant Raman shift of the bond occurs, playing an active role in hydrogen bond formation. The Raman vibrational mode at 312.5 cm^{-1} involves bending of the N₁C₆–NH₂ bond and C₅C₆–NH₂ bond (the number in the prefix symbolizes the position in the adenine group chain). Upon hydrolysis, a greater shift in this bending mode occurs due to the formation of the hydrogen bond. The ribose ring in ATP occurs as a weak Raman active mode and is visible as smeared out peaks in the range from 530.3 to 558.1 cm^{-1} .³² Hydrolysis of ATP enhances the vibrational mode in the ribose ring and can be due to perturbation of other vibrational modes associated with the ribose ring. The sharp feature at 699.0 cm^{-1} is a feature of out-of-plane wagging of NH₂ bonds. The vibrational frequency of 721.1 cm^{-1} in ATP corresponds to the adenine ring breathing mode when all 12 bonds stretch in phase.^{26,33} It can also be due to vibration of D.N₉R and N₃C₄ bonds (where, R represents

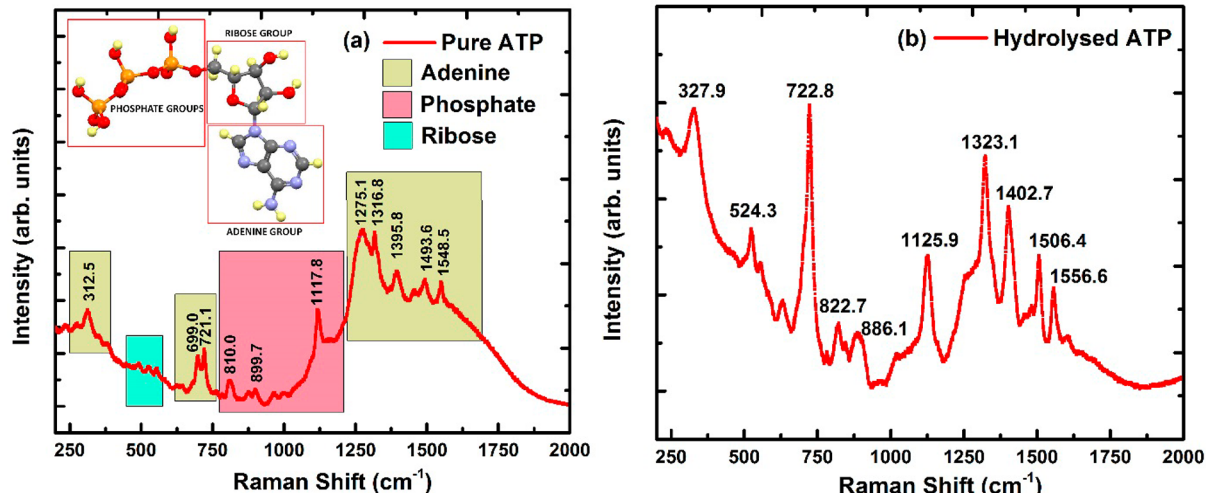


Figure 2. Raman spectra of (a) pure ATP and (b) hydrolyzed ATP.

the ribose ring).²⁰ Hydrolysis of ATP introduces a change in the structural vibrational modes, and the adenine ring modes are mostly affected. This can be inferred from the merging of the two characteristic vibrational modes of the adenine ring to 722.8 cm^{-1} . The hydrogen bonds formed at the NH_2 site annihilate the out-of-plane wagging vibrations in this entity. The Raman shift of the mode associated with the ribose ring introduces a sharp feature of the ribose ring at 524.3 cm^{-1} after hydrolysis. The phosphate moieties play an important role in ATP interaction kinetics and have distinguishable features in Raman spectra. All the vibrational frequencies ranging from 810.0 to 901 cm^{-1} represent phosphate stretching modes ($\text{O}-\text{P}-\text{O}$) present in the ATP biomolecule.²² Small changes in these vibrational modes indicate insurgency during the process of hydrolysis. The peak corresponding to wavenumber 1117.8 cm^{-1} indicates the two phosphate stretching vibrations in the ATP biomolecule.³⁴ The adenine vibrations are the most prominent in the ATP molecule and form the backbone of vibrations ranging from 1000 to 1750 cm^{-1} . The peak at 1275.1 cm^{-1} constitutes the stretching modes of C_8N_7 , C_8N_9 , and N_1C_2 bonds and bending modes of N_1C_2 and C_2H bonds.³⁵ The vibrational mode at 1316.8 cm^{-1} indicates stretching vibrations of N_9C_8 and N_3C_2 bonds and bending vibrations of C_8H and C_2H bonds. Hydrolysis of ATP smears out the 1275.1 and 1316 cm^{-1} peaks to form a new peak at 1323.1 cm^{-1} . The sharp peak feature upon hydrolysis at 1323 cm^{-1} help to propose the reaction energetics of the ATP biomolecule at the N_7 atom by the process of methylation. The peak at 1395.8 cm^{-1} is assigned to vibrations due to C_5N_7 and C_8N_9 bonds.³⁴ The 1493.6 cm^{-1} peak is due to vibrations pertaining to stretching of the C_4N_9 bond and bending of the C_8H bond. The peak at 1548.5 cm^{-1} is a characteristic feature of vibrations of N_3C_4 and C_4C_5 bonds in the adenine entity.³⁶ These vibrations of the adenine ring undergo a change in vibrational frequency due to the formation of hydrogen bonding at the NH_2 site.

Effect of ZnO Nanostructures on the Molecular Vibrational Modes of ATP. Parts b–d of Figure 3 represent the Raman spectra of interacting samples (B, C, and D) under different acidic environments. The ring vibrations of the adenine moiety at 1333.1 , 1367.5 , 1484.9 , and 1572.9 cm^{-1} (in sample B) upon acidification are drastically changed to 1324.0 , 1361.4 , 1494.0 , and 1573.9 cm^{-1} (in sample C) upon protonation at N_1 .^{36,37} These are the characteristic vibrational peaks of the

adenine ring, and a significant Raman shift occurs upon interaction with acid and ZnO nanostructures. According to the literature, further acidification does not change these vibrational modes.²² Our study indicates a considerable change in vibrational frequency to 1325.0 , 1380.7 , 1498.0 , and 1571.5 cm^{-1} (in sample D). These Raman shifts indicate an interaction of ATP with ZnO nanostructures aided by an acidic medium. The shoulder peak at 1519.3 cm^{-1} (in sample C) smears out upon further acidification and is prominent only under slightly acidic conditions. This peak is due to N_7C_8 , C_8N_9 , and $\text{D.C}_8\text{D}$ bonds.³⁸ The N_7 atom in the adenine ring plays an important role in binding kinetics,^{39,40} and the presence of this peak presumes that the N_7 atom also binds to ZnO nanostructures. The ring vibrations at 1484.9 and 1510 cm^{-1} (in sample B) assigned primarily to the five-membered ring were blue-shifted by $\sim 9\text{ cm}^{-1}$ to form peaks at 1494.0 and 1519.3 cm^{-1} (in sample C). This implies that the N_7 position of the adenine ring may be the site of interaction. The red shift and broadening at 1333.1 and 722.9 cm^{-1} (in sample B) may be the result of this interaction since it is known that these two vibrations have contributions from both vibrational and breathing modes in the adenine ring. The red shift is an indication of damped stretching vibrations in the adenine rings.

The interaction was carried out in an acidic medium (using HCl). Acidic environments were used to stabilize the phosphate groups as they are normally negatively charged and unstable due to the presence of highly electronegative oxygen entities in the near vicinity. The three primary phosphate hydrogens are quite acidic and are considered completely ionized at pH greater than 2.0. The terminal phosphate has a pK value of 6.9.^{37,41} Thus, the symmetric stretching vibration of the triphosphate group is shifted from 1123.6 cm^{-1} (in sample B) to 1144.9 cm^{-1} (in sample C) with acidification. On further acid treatment (in sample D) the shift is not considerably larger, indicating complete ionization of the phosphate groups. The blue shift and increase in fwhm of the phosphate stretch peak are also indicative of ZnO nanostructures binding at those active sites. Thus, it appears that the sites of interaction in ATP complexes are only at the triphosphate moiety. Ionization of the triphosphate entities in acidic solution increases the binding characteristics of the nanostructures onto these sites. The larger blue shift is often recorded as increased binding strengths with the phosphate entities. It should also be noted that the blue shift

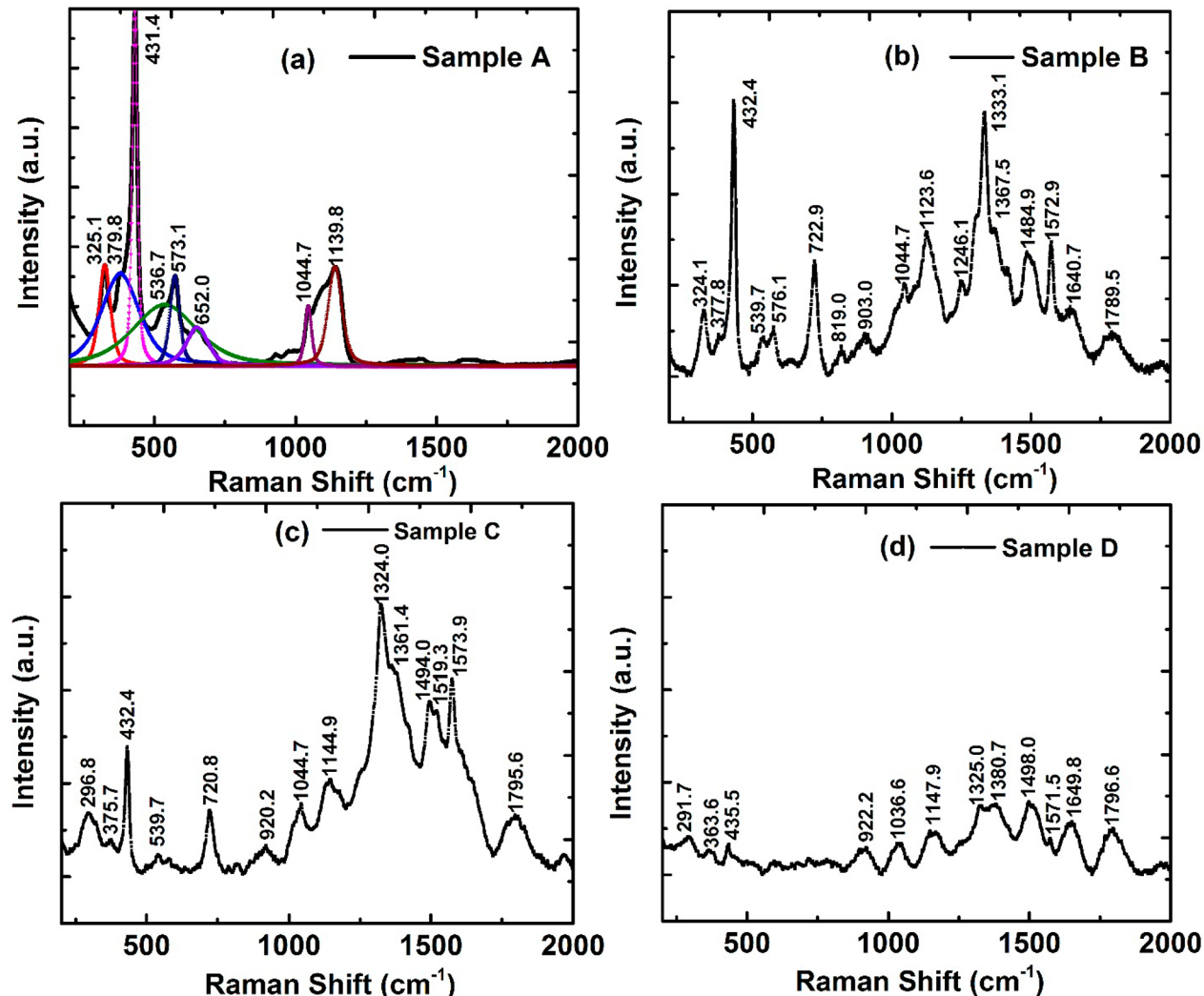


Figure 3. Raman spectra of (a) sample A, (b) sample B, (c) sample C, and (d) sample D.

is not too prominent when more acid is added, which indicates a saturation or denaturation of the active sites.

The spectral changes, particularly the frequency, are too small to suggest a direct coordination of ZnO to N₇. One possibility is that N₇ and the metal ion are separated by an inner sphere water molecule, as suggested by several NMR investigators. Additional interaction with the adenine moiety may be reflected in the red shift and increased peak width at 312.5 cm^{-1} (in pure ATP) to 296.8 cm^{-1} (in sample C), which involve stretching and bending of the $-\text{NH}_2$ bond. The best explanation for our results is that ZnO binds to N₇ and possibly the amino group of ATP not directly, but through a bridging water molecule. The main spectral indication for the N₉-substituted complex is the presence of a relatively strong band at about 1250 cm^{-1} in the Raman spectrum.⁴² Indeed, this band is missing in our Raman spectrum of ZnO interacting with ATP in acidic solutions, suggesting that N₉ is not only H bonded but also substituted through its lone pair of electrons.²²

Raman Spectrum of ZnO Nanostructures. Figure 4 represents the Raman spectra of ZnO nanostructures synthesized by the hydrothermal process, which is being used in further interaction studies. The ZnO crystallographic structure belongs to space group C_{6v} having two formula units for each primitive cell. There all Zn and O atoms occupy

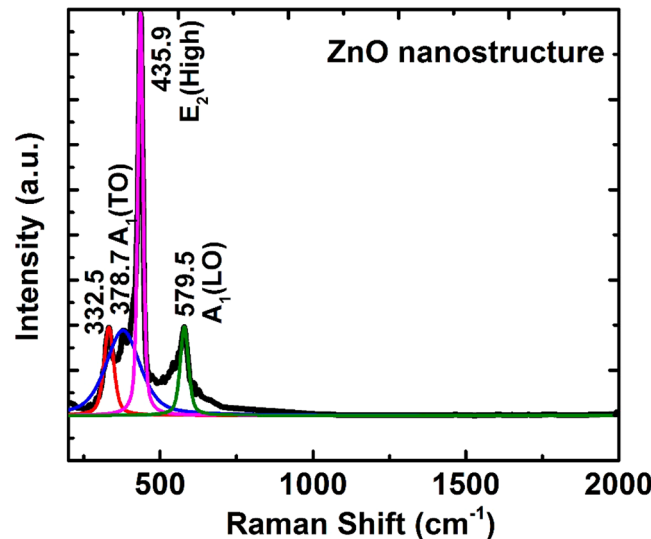


Figure 4. Raman spectra of ZnO nanostructures synthesized by the hydrothermal process. The Voigt peak fittings were performed using Lab spec 5 software.

C_{3v} sites. Group theory predicts $\text{A}_1 + 2\text{E}_2 + \text{E}_1$ are the Raman active vibrational modes in these structures. The polar phonons

A_1 and E_1 exhibit quite different frequencies for transverse optical (TO) modes. ZnO crystals have an E_2 (high) vibrational mode associated with oxygen atoms and an E_2 (low) vibrational mode associated with the Zn sublattice.⁴³ In Figure 4 we present a typical nonresonant Raman scattering spectrum from ZnO nanostructures obtained under 785 nm nonresonant excitation. The analysis of the data presented in Figure 4 indicates that the phonon peak position is consistent for all the different locations and the only difference in the peak intensity comes from the different amounts of ZnO nanostructures in the interaction volume. The observed Raman shifts for the nanostructures are due to the optical phonon confinement effect, which is predominantly larger for nanostructures. Richter et al.⁴⁴ showed that the Raman spectra of nanocrystalline semiconductors are red-shifted and broadened due to the relaxation of the \mathbf{q} vector selection rule. According to the Heisenberg uncertainty principal, the fundamental $\mathbf{q} \approx 0$ Raman selection rule is relaxed for a finite size domain, introducing the contribution of phonons away from the Brillouin zone center. The phonon wave vector uncertainty goes approximately as $\Delta\mathbf{q} \approx 1/D$, where D signifies the diameter of a nanocrystal.^{44,45} This optical phonon spatial confinement introduces the red shift and asymmetric broadening of Raman active peaks. When the grain size increases, Raman peaks become stronger and sharper and shift slightly to higher wavenumber in the case of sample B. The frequency-dependent Raman peak intensity $I(\omega)$ is given by⁴⁶

$$I(\omega) = \int \frac{|C(0, k)|^2}{[\omega - \omega(k)]^2 + (\Gamma_0/2)^2} d^3k \quad (1)$$

where $\omega(k)$ is the phonon dispersion curve, Γ_0 is the natural full line width, and $C(0, k)$ is the Fourier coefficient of the phonon confinement function, which is often represented as

$$|C(k)|^2 = e(-k^2 d^2 / 16\pi^2) \quad (2)$$

where d is the average size of the nanocrystals.⁴⁷ Integrating the above-mentioned equation broadens and red shifts the Raman peaks with decreasing size of the crystals. Crystal defects also cause a change in the Raman frequency. Oxide nanomaterials in particular have many structural defects (oxygen vacancies) which affect their optical properties. The nonpolar optical phonon, E_2 (high), can be red-shifted and strongly broadened for the small quantum dots. The Raman spectroscopy results indicate that the detectable red shifts in ZnO nanostructures are due to the optical phonon confinement. Some of these shifts are due to either defects in the lattice or large size dispersion, which leads to the contribution to the spectrum from smaller diameter nanostructures.

Effect of ATP on Molecular Vibrational Modes of ZnO Nanostructures. The peak that appears at 332.5 cm⁻¹ (in pure ZnO) has been assigned as a second-order mode of Raman scattering in ZnO. Also the peaks at 536.7, 652.0, 1044.0, and 1139.8 cm⁻¹ (in sample A) are predominantly referred to as second-order Raman microscattering and have a lot to tell about the crystal structure of ZnO nanostructures. These processes presumably occur for phonon wave vectors considerably removed from the center of the Brillouin zone. The Raman spectrum also shows peaks at 332.5 and 536.7 cm⁻¹ and can be assigned to the second-order Raman spectrum arising from zone-boundary phonons 2-E₂M and 2-LA(M), respectively.⁴⁸ Phonons confined in nanostructures due to the $\mathbf{q} = 0$ selection rule for first-order Raman scattering is relaxed, and optical phonons at points other than at the zone center

have Raman signals. This ultimately leads to changes in the peak characteristics at low-frequency vibrational phonon modes. Surface-activated optical phonons are also predominant in nanosized materials owing to the considerable particles residing on their surface. The A_1 phonon is polarized parallel to the z axis, while the E_1 phonons are polarized in the xy plane. The Lyddane-Sachs-Teller relation holds that the electrostatic forces in polar cubic crystals generate two transverse branches and one longitudinal branch.⁴⁹ The Lyddane-Sachs-Teller relationship to uniaxial crystals leads to lifting of the 2-fold degeneracy of the E_1 phonons except for phonon propagation along the z axis. Phonon propagation in the xy plane will comprise an A_1 transverse, E_1 transverse, and E_1 longitudinal wave. On account of the anisotropic force constants, the A_1 transverse phonon will have a frequency different from that of an E_1 transverse phonon. The E_1 transverse phonon can be considered a transverse ordinary phonon owing to the fact that its polarization will always be normal to its propagation direction and z axis. The other two phonons could in arbitrary directions be mixtures of transverse and longitudinal waves. Since electrostatic forces are much greater than anisotropic forces, the frequencies of the extraordinary waves will be considerably separated such that there will be minimal mixing of transverse and longitudinal waves. The nature of the electron-phonon coupling introduces the difference in the peak intensity values. In the case of transverse waves only the deformation potential coupling predominates, whereas in the case of longitudinal waves electrostatic coupling plays an active role. Owing to the same contributions to the order of magnitude, it can be additive or subtractive. The changes in polarizability values and Raman peak intensities due to the longitudinal and transverse phonons can be significantly different.³³ The dampening and Raman shifts of the ZnO phonon modes indicate interaction of the ZnO nanostructures with ATP.

Scanning Electron Microscopy (SEM) and Electron Dispersive X-ray Spectroscopy (EDS) Studies of the Samples. It is clearly evident from the SEM images as depicted in Figure 5 that the ATP biomolecule adheres onto the hydrothermally synthesized ZnO nanostructures. Figure 5a shows the rod-shaped ZnO nanostructures, which are also confirmed by EDS studies ($Zn:O \approx 1:1$). With an increase in acidity, the ATP interacts with the ZnO 1D nanorods and is seen to stick to these nanostructures. The phosphorus content is observed in EDS studies and represented in Table 1. It shows an increase in P content with an increase in acidic content. The SEM-EDS mapping image as shown in the Supporting Information clearly shows the presence of phosphorus on the ZnO nanostructures.

Calculation of Molecular Force Constants of Bonds. The fundamental equation for calculating the frequency (f) of vibrations in chemical bonds is given by

$$f = \frac{1}{2\pi} \sqrt{\frac{k}{\mu}} \quad (3)$$

where k is the molecular force constant and μ is the reduced mass and is given by

$$\mu = \frac{m_1 m_2}{m_1 + m_2} \quad (4)$$

where m_1 and m_2 are the masses of the two atoms connected by the chemical bond.

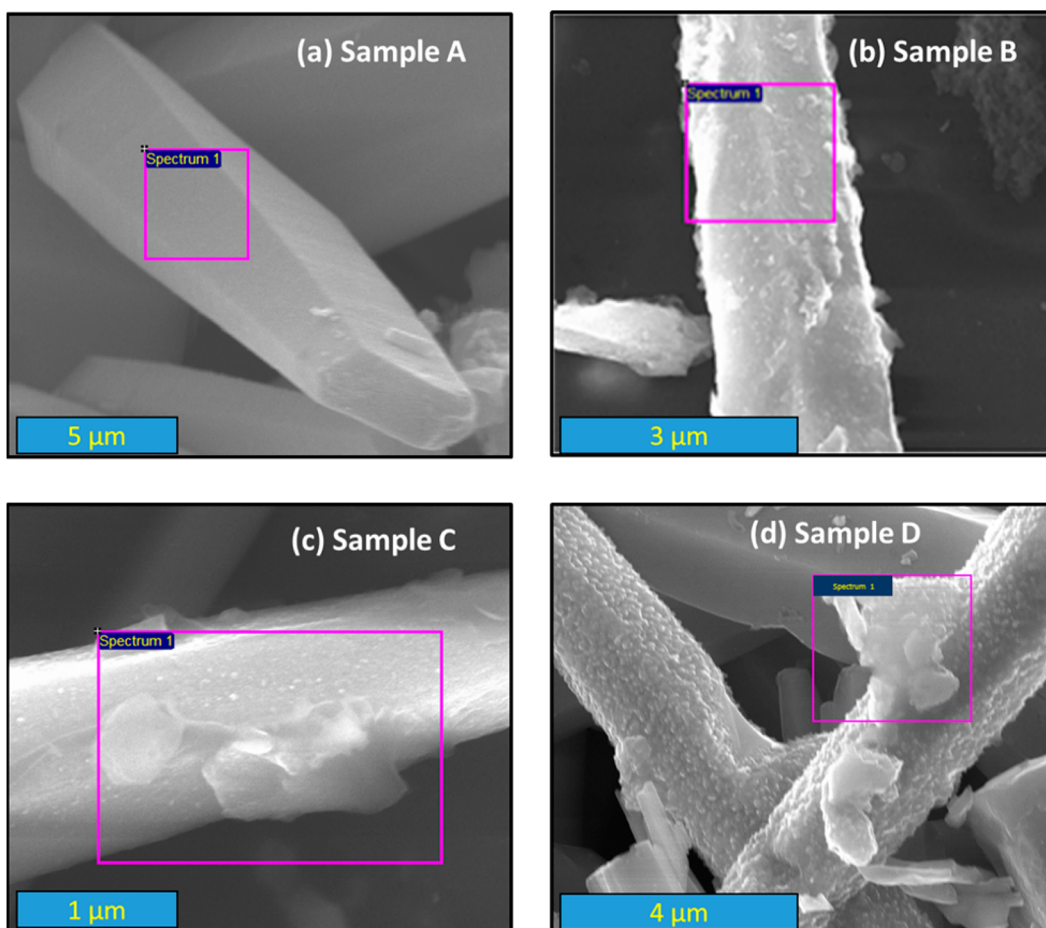


Figure 5. SEM images of (a) sample A, (b) sample B, (c) sample C, and (d) sample D.

Table 1. Observed Concentrations (atom %) of the Elements by EDS

sample	Zn concn	O concn	P concn
A	49.48	50.52	0
B	32.60	64.93	2.57
C	24.57	67.77	6.66
D	19.54	72.12	8.34

The Raman shift (red or blue) is due to the change of the molecular force constants due to interaction. Again the wavenumber ($1/\lambda$) is equal to f/c . The detailed Raman spectroscopic analysis indicates considerable changes in the wavenumbers of the NH_2 bond in the adenine ring (due to water molecule interaction), the N_7 atom in the adenine ring (interaction with Zn^{2+}), and phosphate bonds (ionization due to the presence of acid). The molecular force constants are calculated from the Raman frequencies for the particular bond and are given in Table 2.

An increase in the molecular force constant implies increased force required to vibrate the corresponding molecular bond. After hydrolysis all the concerned molecular bonds are strained as an increase in the force constant occurs. The hydrolyzed sample thus provides a unique environment to test the interaction kinematics of the different functional groups present in the ATP biomolecule. In sample B, ZnO interacts with the hydrolyzed ATP. As proposed earlier, the Zn^{2+} preferentially interacts with the N_7 atom in the adenine ring, and thereby, a decrease of the force constant associated with this molecular bond occurs, which is seen in the case of sample B. With an

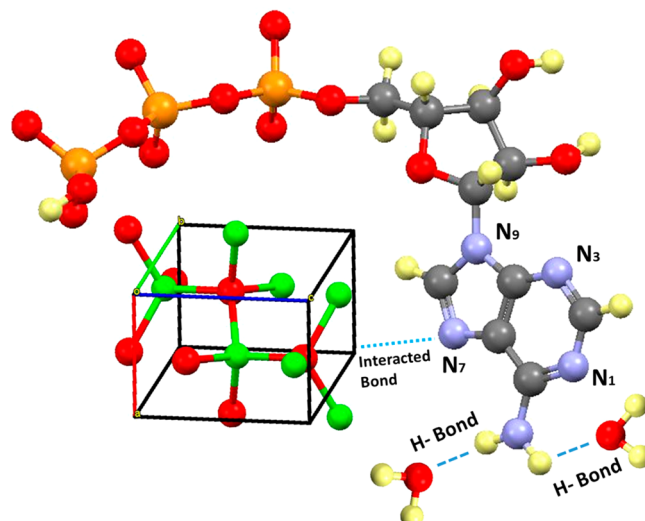


Figure 6. Interaction model of ZnO nanostructures with ATP biomolecule. The black balls represent C, blue balls represent N, yellow balls represent H, red balls represent O, orange balls represent P, and green balls represent Zn.

increase in the acidity, the increased force constant implies restricted vibrations, which can be caused by interaction. The phosphate bonds as mentioned earlier interact with the acid more strongly and become ionized. A slight change in the force constant in the P–O bond occurs with the addition of ZnO in

Table 2. Calculated Molecular Force Constants

name of the bond	ATP		hydrolyzed ATP		sample B		sample C		sample D	
	1/λ (cm⁻¹)	k (N/m)	1/λ (cm⁻¹)	k (N/m)	1/λ (cm⁻¹)	k (N/m)	1/λ (cm⁻¹)	k (N/m)	1/λ (cm⁻¹)	k (N/m)
NH ₂ bond in adenine ring	312.5	5.4	327.9	5.9	324.1	5.7	296.8	4.8	291.7	4.7
N ₇ atom in adenine ring	1493.6	849.3	1506.4	863.9	1484.4	839.5	1494.0	849.8	1498.0	854.3
phosphate bonds	1117.8	776.9	1125.9	788.2	1123.6	785.0	1144.9	815.1	1147.9	819.3

the solution, which is reflected in sample B. In sample C, upon interaction with acid, ionization of the phosphate bonds occurs and is clearly visible by the change in molecular force constant from sample B to sample C. Ionization is complete in this acidic environment, and thereby, there is a minimal change upon addition of more acid. The NH₂ bond force constant increases with hydrolysis of ATP and thereby decreases further with the addition of acid, indicating an interaction with the water molecule via hydrogen bonding. The Raman shift of the ATP is due to its binding with ZnO, thereby causing phonon hardening of the Raman vibrations of ATP. Bulk ATP would have shown no change in Raman frequency, and thereby, the Raman shift would be negligible.

CONCLUSIONS

Nano–bio interaction in nanoconjugates of an energy biomolecule, ATP, and ZnO nanostructures has been investigated using micro Raman spectroscopy, XRD, and electron microscopy. Our results suggest that ATP forms chelate complexes with Zn²⁺; i.e., not only phosphate but also the adenine moiety is involved in the binding reactions. Raman shifts in adenine-related modes are observed when ZnO nanostructures interact with ATP under acidic environments. Zn²⁺ interacts with the adenine moiety of ATP at the N₇ position. Figure 6 pictorially depicts the interaction model of the ZnO nanostructure with the ATP biomolecule. Raman spectroscopy results also indicate a Raman shift when the NH₂ group in the adenine ring facilitates hydrogen bonding with water molecules and the phosphate groups are ionized by the acidic solution. A considerable change in the molecular bond force constants which was calculated from Raman spectroscopy also occurs. This proves the versatility of Raman spectroscopy in probing the interaction characteristics at the nano–bio interface. According to our present study, we conclude that a better understanding of the mechanisms at the nano–bio interface, together with appropriate workmanship, will allow us to make more knowledgeable decisions regarding the interaction kinetics in structurally related nano–bio junctions.

ASSOCIATED CONTENT

Supporting Information

SEM–EDS mapping of a sample showing the presence of P on the ZnO nanorods. This material is available free of charge via the Internet at <http://pubs.acs.org>.

AUTHOR INFORMATION

Corresponding Author

*E-mail: kartikghosh@missouristate.edu.

Notes

The authors declare no competing financial interest.

ACKNOWLEDGMENTS

This research was supported by the National Cancer Institute (Grant 1R15 CA139390-01).

REFERENCES

- (1) Nel, A.; Xia, T.; Mädler, L.; Li, N. Toxic Potential of Materials at the Nanolevel. *Science* **2006**, *311*, 622–627.
- (2) Oberdörster, G.; Maynard, A.; Donaldson, K.; Castranova, V.; Fitzpatrick, J.; Ausman, K.; Carter, J.; Karn, B.; Kreyling, W.; Lai, D.; et al. Principles for Characterizing the Potential Human Health Effects from Exposure to Nanomaterials: Elements of a Screening Strategy. *Part. Fibre Toxicol.* **2005**, *2*, 8.
- (3) Vertegel, A. A.; Siegel, R. W.; Dordick, J. S. Silica Nanoparticle Size Influences the Structure and Enzymatic Activity of Adsorbed Lysozyme. *Langmuir* **2004**, *20*, 6800–6807.
- (4) So, M.-K.; Xu, C.; Loening, A. M.; Gambhir, S. S.; Rao, J. Self-Illuminating Quantum Dot Conjugates for in Vivo Imaging. *Nat. Biotechnol.* **2006**, *24*, 339–343.
- (5) Gilbert, B.; Huang, F.; Zhang, H.; Waychunas, G. A.; Banfield, J. F. Nanoparticles: Strained and Stiff. *Science* **2004**, *305*, 651–654.
- (6) Min, Y.; Akbulut, M.; Kristiansen, K.; Golani, Y.; Israelachvili, J. The Role of Interparticle and External Forces in Nanoparticle Assembly. *Nat. Mater.* **2008**, *7*, 527–538.
- (7) Velegol, D. Assembling Colloidal Devices by Controlling Interparticle Forces. *J. Nanophotonics* **2007**, *1*, 012502.
- (8) Nel, A. E.; Mädler, L.; Velegol, D.; Xia, T.; Hoek, E. M. V.; Somasundaran, P.; Klaessig, F.; Castranova, V.; Thompson, M. Understanding Biophysicochemical Interactions at the Nano-Bio Interface. *Nat. Mater.* **2009**, *8*, 543–557.
- (9) Sundaresan, A.; Bhargavi, R.; Rangarajan, N.; Siddesh, U.; Rao, C. Ferromagnetism as a Universal Feature of Nanoparticles of the Otherwise Nonmagnetic Oxides. *Phys. Rev. B* **2006**, *74*, 161306.
- (10) Zhou, J.; Xu, N. S.; Wang, Z. L. Dissolving Behavior and Stability of ZnO Wires in Biofluids: A Study on Biodegradability and Biocompatibility of ZnO Nanostructures. *Adv. Mater.* **2006**, *18*, 2432–2435.
- (11) Ito, M. In Vitro Properties of a Chitosan-Bonded Hydroxyapatite Bone-Filling Paste. *Biomaterials* **1991**, *12*, 41–45.
- (12) Orstavik, D.; Hongslo, J. K. Mutagenicity of Endodontic Sealers. *Biomaterials* **1985**, *6*, 129–132.
- (13) Gong, M.; Yang, Z.; Xu, X.; Jasion, D.; Mou, S.; Zhang, H.; Long, Y.; Ren, S. Superhydrophobicity of Hierarchical ZnO Nanowire Coatings. *J. Mater. Chem. A* **2014**, *2*, 6180.
- (14) Huang, Z.; Zheng, X.; Yan, D.; Yin, G.; Liao, X.; Kang, Y.; Yao, Y.; Huang, D.; Hao, B. Toxicological Effect of ZnO Nanoparticles Based on Bacteria. *Langmuir* **2008**, *24*, 4140–4144.
- (15) Alim, K. A.; Fonoberov, V. A.; Shamsa, M.; Balandin, A. A. Micro-Raman Investigation of Optical Phonons in ZnO Nanocrystals. *J. Appl. Phys.* **2005**, *97*, 124313.
- (16) Rumyantseva, A.; Kostcheev, S.; Adam, P.-M.; Gaponenko, S. V.; Vaschenko, S. V.; Kulakovitch, O. S.; Ramanenka, A. a; Guzatov, D. V.; Korbutyak, D.; Dzhagan, V.; et al. Nonresonant Surface-Enhanced Raman Scattering of ZnO Quantum Dots with Au and Ag Nanoparticles. *ACS Nano* **2013**, *7*, 3420–3426.
- (17) Baruah, S.; Dutta, J. Hydrothermal Growth of ZnO Nanostructures. *Sci. Technol. Adv. Mater.* **2009**, *10*, 013001.
- (18) Amin, G.; Asif, M. H.; Zainelabdin, A.; Zaman, S.; Nur, O.; Willander, M. Influence of pH, Precursor Concentration, Growth Time, and Temperature on the Morphology of ZnO Nanostructures Grown by the Hydrothermal Method. *J. Nanomat.* **2011**, *2011*, 1–9.
- (19) Whatley, F. R.; Allen, M. B.; Trebst, A. V.; Arnon, D. I. Photosynthesis by Isolated Chloroplasts IX. Photosynthetic Phosphorylation and CO(2) Assimilation in Different Species. *Plant Physiol.* **1960**, *35*, 188–193.

- (20) Zhelyaskov, V.; Yue, K. T. A Raman Study of the Binding of Fe(III) to ATP and AMP. *Biochem. J.* **1992**, *287* (Part 2), 561–566.
- (21) Lanir, A.; Yu, N. T. A Raman Spectroscopic Study of the Interaction of Divalent Metal Ions with Adenine Moiety of Adenosine 5'-Triphosphate. *J. Biol. Chem.* **1979**, *254*, 5882–5887.
- (22) Rimai, L.; Cole, T.; Parsons, J. L.; Hickmott, J. T.; Carew, E. B. Studies of Raman Spectra of Water Solutions of Adenosine Tri-, Di-, and Monophosphate and Some Related Compounds. *Biophys. J.* **1969**, *9*, 320–329.
- (23) Uskoković-Marković, S.; Jelikić-Stankov, M.; Holclajtner-Antunović, I.; Đurđević, P. Raman Spectroscopy as a New Biochemical Diagnostic Tool. *J. Med. Biochem.* **2013**, *32*, 96–103.
- (24) Uetsuki, K.; Verma, P.; Yano, T.; Saito, Y.; Ichimura, T.; Kawata, S. Experimental Identification of Chemical Effects in Surface Enhanced Raman Scattering of 4-Aminothiophenol. *J. Phys. Chem. C* **2010**, *114*, 7515–7520.
- (25) Hu, X.; Wang, T.; Wang, L.; Dong, S. Surface-Enhanced Raman Scattering of 4-Aminothiophenol Self-Assembled Monolayers in Sandwich Structure with Nanoparticle Shape Dependence: Off-Surface Plasmon Resonance Condition. *J. Phys. Chem. C* **2007**, *111*, 6962–6969.
- (26) McCusker, L. B.; Von Dreele, R. B.; Cox, D. E.; Louër, D.; Scardi, P. Rietveld Refinement Guidelines. *J. Appl. Crystallogr.* **1999**, *32*, 36–50.
- (27) Cheary, R. W.; Coelho, A. A Fundamental Parameters Approach to X-Ray Line-Profile Fitting. *J. Appl. Crystallogr.* **1992**, *25*, 109–121.
- (28) Rimai, L.; Heyde, M. E.; Carew, E. B. Effect of Divalent Metal Ion Binding on the Raman Spectrum of ATP in Aqueous Solution. *Biochem. Biophys. Res. Commun.* **1970**, *38*, 231–237.
- (29) Rimai, L.; Heyde, M. E. An Investigation by Raman Spectroscopy of the Base-Proton Dissociation of ATP in Aqueous Solution and the Interactions of ATP with Zn⁺⁺ and Mn⁺⁺. *Biochem. Biophys. Res. Commun.* **1970**, *41*, 313–320.
- (30) Rimai, L.; Heyde, M. E. Raman Spectroscopic Study of the Interaction of Ca²⁺ and Mg²⁺ with the Triphosphate Moiety of Adenosine Triphosphate in Aqueous Solution. *Biochemistry* **1971**, *10*, 1121–1128.
- (31) Yu, N.-T.; Krimm, S. Raman Spectroscopy: A Conformational Probe in Biochemistry. *Crit. Rev. Biochem. Mol. Biol.* **1977**, *4*, 229–280.
- (32) Hamada, Y. Z.; Greene, J. T.; Shields, V.; Pratcher, M.; Gardiner, S.; Waddell, E.; Shreeves, S.; Sunda-Meya, A.; Phambu, N. Spectroscopic and Potentiometric Studies of the Interaction of Adenine with Trivalent Metal Ions. *J. Coord. Chem.* **2010**, *63*, 284–295.
- (33) Majoube, M. Adenine Residue: A Normal-Coordinate Analysis of the Vibrational Spectra. *Biopolymers* **1985**, *24*, 2357–2369.
- (34) Forrest, G.; Lord, R. C. Laser Raman Spectroscopy of Biomolecules. X-Frequency and Intensity of the Phosphodiester Stretching Vibrations of Cyclic Nucleotides. *J. Raman Spectrosc.* **1977**, *6*, 32–37.
- (35) Chinsky, L.; Turpin, P. Y. Ultraviolet Resonance Raman Study of DNA and of Its Interaction with Actinomycin D. *Nucleic Acids Res.* **1978**, *5*, 2969–2978.
- (36) Khalil, F. L.; Brown, T. L. Infrared Spectra of Adenosine Triphosphate Complexes in Deuterium Oxide Solution. *J. Am. Chem. Soc.* **1964**, *86*, 5113–5117.
- (37) Alberty, R. A. Effect of pH and Metal Ion Concentration on the Equilibrium Hydrolysis of Adenosine Triphosphate to Adenosine Diphosphate. *J. Biol. Chem.* **1968**, *243*, 1337–1343.
- (38) Lewis, A.; Nelson, N.; Racker, E. Laser Raman Spectroscopy as a Mechanistic Probe of the Phosphate Transfer from Adenosine Triphosphate in a Model System. *Biochemistry* **1975**, *14*, 1532–1535.
- (39) Swift, T. J.; Glassman, T. A.; Cooper, C.; Harrison, L. W. Proton Magnetic Resonance Study of Metal-Ion-Adenine Ring Interactions in Metal Ion Complexes with Adenosine Triphosphate. *Biochemistry* **1971**, *10*, 843–851.
- (40) Kuntz, G. P.; Glassman, T. A.; Cooper, C.; Swift, T. J. The Role of Coordinated Water in Metal Ion–Adenine Ring Binding in Complexes of Adenosine Triphosphate. *Biochemistry* **1972**, *11*, 538–541.
- (41) Takeuchi, H.; Murata, H.; Harada, I. Interaction of Adenosine 5'-Triphosphate with Mg²⁺ Vibrational Study of Coordination Sites by Use of O-Labeled Triphosphates. *J. Am. Chem. Soc.* **1988**, *110*, 392–397.
- (42) Tajmir-Riahi, H. A.; Langlais, M.; Savoie, R. A Laser Raman Spectroscopic Study of the Interaction of the Methylmercury Cation with AMP, ADP and ATP. *Biochim. Biophys. Acta, Protein Struct. Mol. Enzymol.* **1988**, *956*, 211–216.
- (43) Arguello, C.; Rousseau, D.; Porto, S. First-Order Raman Effect in Wurtzite-Type Crystals. *Phys. Rev.* **1969**, *181*, 1351–1363.
- (44) Richter, H.; Wang, Z. P.; Ley, L. The One Phonon Raman Spectrum in Microcrystalline Silicon. *Solid State Commun.* **1981**, *39*, 625–629.
- (45) Rajalakshmi, M.; Arora, A. K.; Bendre, B. S.; Mahamuni, S. Optical Phonon Confinement in Zinc Oxide Nanoparticles. *J. Appl. Phys.* **2000**, *87*, 2445.
- (46) Huang, K. The Long Wave Modes of the Cu₂O Lattice. *Z. Phys.* **1963**, *171*, 213–225.
- (47) Xu, J. F.; Ji, W.; Shen, Z. X.; Li, W. S.; Tang, S. H.; Ye, X. R.; Jia, D. Z.; Xin, X. Q. Raman Spectra of CuO Nanocrystals. *J. Raman Spectrosc.* **1999**, *30*, 413–415.
- (48) Calleja, J.; Cardona, M. Resonant Raman Scattering in ZnO. *Phys. Rev. B* **1977**, *16*, 3753–3761.
- (49) Damen, T.; Porto, S.; Tell, B. Raman Effect in Zinc Oxide. *Phys. Rev.* **1966**, *142*, 570–574.